Annular flow instabilities and large-scale vortices in electromagnetically driven horizontal soap films

Andrey Pototsky,[1,*] Aldo Figueroa,[2] José Olvera-Orozco,[3] Misael Álvarez-Jiménez,[4] Sergio Cuevas,[3] and Sergey A. Suslov[1]

[1]*Department of Mathematics, Swinburne University of Technology, Hawthorn, Victoria 3122, Australia*
[2]*Conahcyt-Centro de Investigación en Ciencias, Universidad Autónoma del Estado de Morelos, Avenida Universidad 1001, Chamilpa, Cuernavaca 62209, Morelos, México*
[3]*Instituto de Energías Renovables, Universidad Nacional Autónoma de México, A.P. 34, Temixco 62580, Morelos, México*
[4]*Instituto de Investigación en Ciencias Básicas y Aplicadas, Universidad Autónoma del Estado de Morelos, Avenida Universidad 1001, Chamilpa, Cuernavaca 62209, Morelos, México*

(Received 1 November 2024; accepted 11 March 2025; published 24 March 2025)

We study the conditions under which large-scale vortex flow patterns appear in electromagnetically driven conducting horizontal soap films created between two coaxial cylindrical electrodes and placed in a vertical magnetic field. For large Marangoni and Peclet numbers, the two-dimensional flow in a flat free film is effectively incompressible and the surface concentration of an insoluble surfactant plays the role of the pressure away from the boundaries. If the direct radial electric current flows through the film, the Lorentz force arising in a uniform field drives the azimuthal flow. Its stability is investigated in cases of slip and no-slip boundary conditions at the edges of the film in the limit of a small Hartmann number. Flow stability changes nontrivially depending on the slip length, and the flow stabilizes for perfect-slip boundaries. In contrast, if the vertical axisymmetric field is strongly nonuniform, the flow may become linearly unstable at much smaller Reynolds numbers than the critical value for no-slip boundaries,- leading to the formation of large-scale circulation cells. Our experiments conducted using a piecewiseconstant magnetic field detect the formation of vortex structures that are in qualitative agreement with those predicted by the performed analysis.

DOI: 10.1103/PhysRevFluids.10.034802

I. INTRODUCTION

The formation of localized vortices in quasi-two-dimensional flows as well as their stability and coalescence dynamics continue to attract much interest due to their importance in geophysical fluid flows [1–3] and the possibility of studying two-dimensional turbulence [4,5]. On the scale of several thousands of kilometers, such vortices typically appear in unbounded oceanic or atmospheric flows as a result of shear, centrifugal, or Coriolis forces and have a lifetime that depends on viscosity and external conditions. Similar two-dimensional circulation flows resembling eddies are also found on a much smaller scale of several centimeters in electrically conducting fluids driven by the Lorentz force that results from the interaction of electric current flowing through the fluid and a nonuniform external magnetic field [6,7]. The vortex structures appear as a result of an instability of a base flow, and the transition from a stable to unstable regime is observed when the Reynolds number increases. However, not all types of steady flows become unstable. For example, a shear flow of a viscous fluid confined between two parallel impermeable solid plates with no slip boundaries sliding with

*Contact author: apototskyy@swin.edu.au

respect to each other (the classical plane Couette flow) is linearly stable irrespective of the Reynolds number [8,9].

The Taylor-Couette flow between two concentric rotating cylinders, while becoming unstable with respect to perturbations that are periodic along the axes of the cylinders, also remains stable with respect to purely azimuthal perturbations [10]. In an attempt to find the class of the steady flow fields that may become unstable and potentially give rise to a turbulent flow regime, Kolmogorov suggested a toy hydrodynamic model based on a two-dimensional flow of viscous incompressible fluid [4], the velocity of which varies harmonically in the transverse direction. Other geometries have been suggested, including a planar rotational axisymmetric flow between two coaxial cylinders [6,7,11]. A comprehensive review of the experimental realizations of the Kolmogorov flow and its stability is given in Ref. [12].

Despite the existence of extensive literature on axisymmetric geophysical and electromagnetically driven flows, only three types of steady two-dimensional circulation flows and their stability have been considered so far. The first type, which is fundamentally important in the context of geophysical studies, is characterized by an axisymmetric distribution of vorticity given by the exact solution of the inviscid barotropic Euler equations [3,13]. Such a solution corresponds to an isolated monopole vortex in an unbounded fluid with the flow velocity decreasing as e^{-r^a} with the distance r from the center of the vortex. It was found that the azimuthal perturbation mode with wave number $n = 1$ of the monopole vortex always decays, while the mode with the wave number $n = 2$ has the largest growth rate. Depending on the decay parameter a, the vortex may be unstable and evolve into either a dipole or a tripole, which are characterized by two (three) vorticity maxima translating as a whole with a constant angular velocity [14,15]. Stable isolated vortices can only exist in the inviscid limit and dissipate over their characteristic lifetime if the viscosity is taken into account. As shown by Oseen and Lamb [16], the velocity field of a dissipating vortex in a viscous fluid decays as $\frac{1}{r}$. A comprehensive review of vortices and their stability in rotating fluids can be found in Refs. [13,17,18].

The second type of steady two-dimensional circular flow that resembles a monopole vortex is found in electromagnetically driven conducting fluids (for example, mercury) confined by two concentric cylinders and placed in an axial magnetic field [19,20]. The flow is generated when an electric current passes through the fluid between a set of coaxial electrodes located at the bottom of the container some distance away from the cylindrical outside walls. Under these conditions, the so-called free layer of rotating fluid is formed, which is fully detached from the side boundaries. The radial distribution of the azimuthal velocity in the layer behaves approximately as $e^{-a(r-r_0)^2}$, where r_0 is the location of the center of the layer and $a \sim \mathrm{Ha}$ is the shape parameter that depends on the applied magnetic field [21]. Assuming that the velocity perturbations satisfy the no-slip boundary conditions at the confining walls, the stability of the base flow was found to be very sensitive to the variations of the Hartmann number. While a comprehensive analysis of the flow instability was not originally reported, it can be deduced that the most dangerous perturbation mode has the wave number $n = 4$. However, these results are only approximate because the assumed base flow does not vanish at the confining walls [21].

The third type of steady circulation that was mentioned in relation to the Kolmogorov flow is that of a viscous fluid confined by two coaxial cylinders with radii r_1 and r_2, $r_1 < r_2$, and driven by a nonuniform body force that had a (somewhat artificial) radial distribution given by $J_1(pr/r_2)$, where J_1 is the Bessel function of the first kind and the parameter p is chosen so that the flow vanishes at $r = r_1, r_2$ [6,11]. This choice of the base flow corresponds to no-slip boundaries. Under the assumption that the flow changes its direction only once in $r_1 \leqslant r \leqslant r_2$, it was shown that the most dangerous perturbation mode is either that with the wave number $n = 2$ in the case of a disk ($r_1 = 0$), or with $n = 3$ in the case of an annulus with $x = pr_1/r_2$ and $x = p$ corresponding to the first and third zeros of $J_1(x) = 0$, respectively.

Previously, experimental investigation of quasi-two-dimensional flows was carried out using thin layers of mercury driven electromagnetically using the Lorentz force. Various geometries have been employed, including thin layers sandwiched between two solid plates [22–24] and horizontal layers supported by a solid bottom with a free upper surface [25]. One of the main challenges of inducing flows involving small amounts of fluids in confined geometries is the necessity to overcome a significant friction force at the boundary. Because of that, stronger magnetic fields and larger electric currents must be used to sustain the flow. The use of free liquid films offers a way of reducing an interfacial friction. In addition, the flow field in films is much closer to two-dimensional than that in thin liquid layers supported by a solid bottom. Therefore, a free film is an excellent candidate for an experimental realization of two-dimensional circulation flows.

Experimentally, mechanically driven flows in horizontal soap films have been used to study the formation of vortices and the onset of turbulence in a two-dimensional geometry [5,26,27]. The flow in the film was induced by viscous coupling with the ambient air that was set in motion by two counterrotating cylinders placed under the film [5]. Reminiscent of the Kelvin-Helmholtz instability in shear flows, the formation of several vortices was observed. Alternatively, an array of steady vortices was created by directing a jet of air perpendicular to the film surface [27]. However, these classical experiments involved an effectively three-dimensional setup because it involved a flow in a film coupled via surface stresses with a three-dimensional motion of the ambient air layer.

In this article, we focus on the stability of a steady rotating flow in free horizontal soap films confined by two coaxial cylinders. The flow is driven by a radially nonuniform axisymmetric Lorentz body force induced by the radial current flowing through the film placed in an external magnetic field. Furthermore, coupling with the ambient air becomes inconsequential, which makes focusing on film flow processes alone methodologically justifiable. Additionally, in the regime characterized by large Marangoni and Péclet numbers, the distribution of the insoluble surfactant on the surface of the film outside of the meniscus zone adjusts almost instantly to changes in the flow field. Under these conditions the film remains approximately flat [28], putting a two-dimensional incompressible flow consideration on an even firmer ground.

In view of these arguments, our aim is to study the stability of the base azimuthal flow driven by the Lorentz force in the flat film between concentric electrodes in the two-dimensional framework. We will consider the cases of uniform and piecewise-constant magnetic fields and investigate the role of the no-slip and partial-slip boundary conditions at the film edges. The former is a standard fluid-solid interface condition. However, on a contact with a solid wall the film necessarily develops a meniscus, where two-dimensional flow consideration is likely to be inadequate. To avoid dealing with a strongly curved meniscus in the model, we view the film as flat everywhere and impose the partial-slip velocity condition at the surface of the cylindrical electrodes.

II. ELECTROMAGNETICALLY DRIVEN FLOW IN A FREE HORIZONTAL FILM LOADED WITH AN INSOLUBLE SURFACTANT

Consider a flat horizontal liquid film with an average thickness $H = 2h_0$ bounded by two interfaces located at $z = \pm h_0$. The interfaces are loaded with insoluble surfactant with the surface concentration c. The electrically conducting fluid forming the film is incompressible and has density ρ, dynamic viscosity μ, electric conductivity σ, and surface tension γ. The film is stretched between two coaxial electrodes and is placed into a (generally nonuniform) vertical magnetic field $\boldsymbol{B} = B_0 f(x, y)\boldsymbol{e}_z$, where B_0 is the field amplitude, $f(x, y)$ is a dimensionless function, and $\boldsymbol{e}_z$ is the unit vector in the vertical direction. When the electric potential difference V is applied between the electrodes, the electric current flows through the film and induces a nonuniform azimuthal Lorentz force that drives the fluid azimuthally. In a typical experimental realization such a flow has a characteristic velocity U ranging from several centimeters to several decimeters per second [29].

Before formulating the equations of fluid motion, we estimate the relative strength of the Marangoni, Lorentz-force-induced, and viscous effects and the surface diffusivity of the surfactant. The Marangoni number is defined as $\mathrm{Ma} = \frac{E}{\mu U}$, where $E = -2c_0 \frac{\mathrm{d}\gamma}{\mathrm{d}c}$ denotes the Marangoni elasticity of a free film loaded with surfactant with average concentration c_0 [30]. Recent experiments estimate the Marangoni elasticity of common soap films at $E = 22$ N/m and find it independent of the film thickness [31]. Related to the Marangoni number is the elastic Mach number $M_e = \frac{U}{U_e}$,

TABLE I. Typical values of dimensionless parameters.

Parameter	Definition	Value range
Marangoni number	$\mathrm{Ma} = \frac{E}{\mu U}$	10^5–10^6
Hartmann number	$\mathrm{Ha} = B_0 L\sqrt{\frac{\sigma}{\mu}}$	10^{-2}–10^{-1}
Péclet number	$\mathrm{Pe} = \frac{LU}{d_s}$	10^4–10^7
Reynolds number	$\mathrm{Re} = \frac{\sigma B_0 V L^2 \rho}{\mu^2}$	0–10^6
Elastic Mach number	$M_e = U\sqrt{\frac{2\rho h_0}{E}}$	10^{-4}–10^{-3}

where $U_e = \sqrt{\frac{E}{2\rho h_0}}$ is the speed of the elastic Marangoni waves propagating along the surface of the film [28]. The Péclet number is given by $\mathrm{Pe} = \frac{LU}{d_s}$, where L is the horizontal length scale and d_s is the surface diffusivity [30]. For foam films stabilized by various surface-active molecules, the diffusivity d_s is in the range 10^{-10}–10^{-8} $\mathrm{m}^2\,\mathrm{s}^{-1}$ [32]. The volumetric density of the Lorentz force is $\boldsymbol{j} \times \boldsymbol{B}$, where $\boldsymbol{j} = \sigma(\boldsymbol{u} \times \boldsymbol{B} - \nabla\phi)$ is the electric current density and $\boldsymbol{u}$ is the fluid velocity. For magnetic fields with a flux density of up to $B_0 \sim 10^{-1}$ T, as typically used in experiments [29,33,34], the ratio of the Lorentz force component $\sigma(\boldsymbol{u} \times \boldsymbol{B}) \times \boldsymbol{B}$ to the viscous stress $\mu\nabla^2\boldsymbol{u}$ is characterized by the Hartmann number $\mathrm{Ha} = B_0 L\sqrt{\frac{\sigma}{\mu}}$. In water-based weak electrolytes such as sodium chloride (NaCl) or sodium bicarbonate ($NaHCO_3$), the characteristic value of Ha^2 is in the range 10^{-4}–10^{-2}, which justifies neglecting the induced component of the Lorentz force. In this limit, the electric current density $\boldsymbol{j} = -\sigma\nabla\phi$, where ϕ is the applied electric potential, is independent of the flow velocity.

The characteristic velocity u_{Lor} of the flow arising due to the action of the Lorentz force is determined by considering the balance between the electrostatic component of the Lorentz force, $-\sigma\nabla\phi \times \boldsymbol{B}$, and the viscous stress, $\mu\nabla^2\boldsymbol{u}$. This gives $u_{\mathrm{Lor}} = \frac{\sigma B_0 V L}{\mu}$. In experiments with water-based weak electrolyte solutions, the applied potential difference V may reach 150 V [29]. The Reynolds number associated with the horizontal flow is defined as $\mathrm{Re} = \frac{u_{\mathrm{Lor}}}{u_{\mathrm{visc}}} = \frac{\sigma B_0 V L^2 \rho}{\mu^2}$, where $u_{\mathrm{visc}} = \frac{\mu}{\rho L}$ is the viscous velocity. Taking $L = 10^{-2}$ m and assuming that the average film thickness $2h_0$ is 1–10 μm, we estimate the ranges of dimensionless parameters in Table I.

The complete set of reduced hydrodynamic equations that describe two-dimensional motion of the fluid and insoluble surfactant in the presence of the Lorentz force was formulated in the lubrication approximation by neglecting gravity and taking into account only varicose deformation modes in Refs. [35,36]. Upon scaling the two-dimensional flow $\boldsymbol{u} = (u_x, u_y)$ with $U = \frac{\sigma B_0 V L}{\mu}$, the horizontal coordinates with L, time with $\frac{L}{U}$, and the electric potential with V, the nondimensional Navier-Stokes equation in the limit of small Hartmann number is written as

$$\partial_t \boldsymbol{u} + (\boldsymbol{u} \cdot \nabla)\boldsymbol{u} = \frac{1}{\mathrm{Re}}(\nabla^2\boldsymbol{u} + 3\nabla(\nabla \cdot \boldsymbol{u}) - f\nabla\phi \times \boldsymbol{e}_z) - \frac{1}{M_e^2}\nabla\hat{c} + O(\nabla\delta\hat{h}), \tag{1}$$

where $\hat{c} = \frac{c}{c_0}$ and $\hat{h} = \frac{h}{h_0}$ are the scaled surfactant concentration and film thickness, respectively. Away from the edges of the film, the Laplace pressure gradient and nonlinear extensional Trouton viscosity [28] are vanishingly small and $\nabla\hat{h} \ll 1$ can be neglected.

In regimes characterized by parameter values listed in Table I, Eq. (1) can be simplified as shown in Ref. [28] in the absence of the Lorentz force. When the elastic Mach number $M_e \ll 1$, the horizontal fluid motion along the film surface away from the boundaries is dominated by the Marangoni flow. Any perturbation of the surfactant concentration relaxes almost instantly to a homogeneously spread monolayer. For large Péclet numbers, the concentration $\hat{c}$ follows the advection equation $\partial_t\hat{c} + \nabla(\hat{c}\boldsymbol{u}) = 0$. Therefore, at the leading order $\hat{c} = 1$, the two-dimensional flow $\boldsymbol{u} = (u_x, u_y)$ at the surface of a flat film becomes effectively incompressible; that is, $\nabla \cdot \boldsymbol{u} = 0$.

The fluid volume conservation implies that $\partial_t \hat{h} + \nabla \cdot (\hat{h}\boldsymbol{u}) = 0$, which along with the condition $\nabla \cdot \boldsymbol{u} = 0$ leads to $\partial_t \hat{h} + \nabla \hat{h} \cdot \boldsymbol{u} = 0$. Consequently, if the film was initially flat, that is, if $\nabla h = 0$, then its surface will remain unperturbed at all times. Therefore, at the leading order $O(M_e^{-2})$, $\hat{c} = \hat{h} = 1$ and $\boldsymbol{u} = 0$.

Finally, upon using $\nabla \cdot \boldsymbol{u} = 0$, Eq. (1) is written as

$$\partial_t \boldsymbol{u} + (\boldsymbol{u} \cdot \nabla)\boldsymbol{u} = -\frac{1}{M_e^2}\nabla \hat{c} + \frac{1}{\mathrm{Re}}(\nabla^2 \boldsymbol{u} + f \nabla \phi \times \boldsymbol{e}_z). \tag{2}$$

This is complemented by the condition of nonaccumulation of an electric charge $\nabla^2 \phi = 0$. As was previously recognized in Refs. [27,28] and as seen from Eq. (2), the surfactant concentration plays the role of pressure in films away from the meniscus zones.

III. TWO-DIMENSIONAL ELECTROMAGNETICALLY DRIVEN ANNULAR FLOW IN A SOAP FILM AND ITS STABILITY

A. Governing equations

We consider the flow in an annular soap film spanning the gap between two coaxial cylindrical electrodes with radii r_1 and $r_2 > r_1$ in an axially symmetric magnetic field $f(x, y) = f(r)$. In what follows we choose the horizontal length scale $L = r_2 - r_1$ so that the scaled radii of the inner and outer cylinders are $\frac{r_1}{L} = \alpha$ and $\frac{r_2}{L} = 1 + \alpha$, respectively. For a vanishing Hartmann number, the electric potential is independent of the fluid velocity and is given by

$$\phi = \frac{\ln(r\alpha^{-1})}{\ln(1 + \alpha^{-1})}. \tag{3}$$

The Navier-Stokes equation (2) and the continuity equation written in polar coordinates (r, θ) with $\boldsymbol{u} = u\boldsymbol{e}_r + v\boldsymbol{e}_\theta$ are

$$\partial_t u + u\partial_r u + \frac{v}{r}\partial_\theta u - \frac{v^2}{r} = \frac{1}{\mathrm{Re}}\left(Du + \frac{\partial_\theta^2 u}{r^2} - \frac{2\partial_\theta v}{r^2}\right) - \frac{1}{M_e^2}\partial_r \hat{c}, \tag{4}$$

$$\partial_t v + u\partial_r v + \frac{v}{r}\partial_\theta v + \frac{vu}{r} = \frac{1}{\mathrm{Re}}\left(Dv + \frac{\partial_\theta^2 v}{r^2} + \frac{2\partial_\theta u}{r^2}\right) + \frac{f(r)}{\mathrm{Re}\, r \ln(1 + \alpha^{-1})} - \frac{1}{M_e^2}\frac{\partial_\theta \hat{c}}{r}, \tag{5}$$

$$\partial_r u + \frac{u}{r} + \frac{\partial_\theta v}{r} = 0, \tag{6}$$

where $D = \partial_r^2 + r^{-1}\partial_r - r^{-2}$. We assume the no-penetration conditions for the radial velocity component and the linear Navier slip boundary conditions for the azimuthal velocity component,

$$u = 0, \quad v = \beta \partial_{\boldsymbol{n}} v, \tag{7}$$

at $r = \alpha$ and $r = 1 + \alpha$, where β is the dimensionless slip length parameter and $\boldsymbol{n}$ is the unit vector normal to the surfaces of the electrodes pointing into the domain occupied by the fluid. Thus, at $r = \alpha$ and $r = 1 + \alpha$, the slip condition becomes $v = \pm\beta\partial_r v$, respectively. Note that the surfactant field can be eliminated from Eq. (2) by taking the curl to obtain

$$\partial_t \omega + \frac{1}{r}(\partial_r \omega \partial_\theta \psi - \partial_\theta \omega \partial_r \psi) = \frac{1}{\mathrm{Re}}\left(\nabla^2 \omega + \frac{1}{r \ln(1 + \alpha^{-1})}\frac{\mathrm{d}f}{\mathrm{d}r}\right), \tag{8}$$

where ψ is the stream function related to the velocity as $u = r^{-1}\partial_\theta \psi$ and $v = -\partial_r \psi$ and $\omega = r^{-1}(v + r\partial_r v - \partial_\theta u) = -\nabla^2 \psi$ is the flow vorticity.

Before proceeding with the analysis of two-dimensional flow described by Eq. (2), we emphasize that an ideally flat horizontal free film bounded by hydrophilic vertical solid walls is metastable due to the border suction mechanism induced by the pressure difference between the region under the curved meniscus (also known as the Plateau border) and a flat part of the film (also known as the lamella) [37,38]. As a result of it, the fluid flows toward the border, leading to film thinning away from the border and its eventual rupture there. In what follows we assume that the characteristic time of the border suction mechanism is much larger than the typical time of flow development under the action of the Lorentz force. In this regime, the no-penetration condition $u = 0$ can be imposed so that the total fluid volume in the film is conserved.

B. Steady azimuthal flow

In the steady state, the flow is purely azimuthal and axisymmetric: $u = 0$, $v = v_0(r)$, $\hat{c} = 1 + M_e^2 c_0(r)$, where $\int_\alpha^{1+\alpha} r c_0(r)\,\mathrm{d}r = 0$. Away from the meniscus zones the Marangoni stress gradient proportional to the gradient of the surfactant concentration compensates for the centrifugal force while the azimuthal Lorentz force drives the flow so that

$$\frac{\mathrm{d}c_0}{\mathrm{d}r} = \frac{v_0^2}{r}, \tag{9}$$

$$\frac{\mathrm{d}^2 v_0}{\mathrm{d}r^2} + \frac{1}{r}\frac{\mathrm{d}v_0}{\mathrm{d}r} - \frac{v_0}{r^2} = -\frac{f(r)}{r\ln(1+\alpha^{-1})}. \tag{10}$$

It follows from Eq. (9) that in the no-slip case, $\beta = 0$, the steady surfactant flux at the boundaries vanishes as expected at the solid walls. If slip is allowed, then $\mathrm{d}c_0/\mathrm{d}r \neq 0$, which implies that the total amount of the surfactant is not conserved.

We emphasize that a consistent hydrodynamic description of the Plateau border region requires careful study of the shape of the meniscus and additional assumptions on the behavior of the contact line between the film and the solid wall [38]. Here we employ a simplified heuristic approach by excluding the meniscus zone from the analysis so that the edge of the considered flow domain effectively remains some distance away from a solid wall. Therefore, complex hydrodynamic and chemical transport processes that may take place in the meniscus zone are not accounted for in the present analysis. The no-slip condition is consistent with the Reynolds model of hydrodynamic lubrication, which assumes no tangential flow at the surface of the bounding walls. On the other hand, the Navier slip condition with $\beta \neq 0$ is used to mimic the Plateau border region, which acts as an effective lubrication layer between the solid wall and lamella.

The general solution of Eq. (10) is

$$v_0 \ln(1+\alpha^{-1}) = g(r) = C_1 r + \frac{C_2}{r} - \frac{F(r)}{r}, \tag{11}$$

where $F(r) = \iint_\alpha^r \frac{f(r')\,\mathrm{d}r'}{r'} r\,\mathrm{d}r$ and $C_{1,2}$ are given by

$$\begin{aligned} C_1 &= E[(F(\alpha) - \beta F'(\alpha))((1+\alpha)^{-1} + \beta(1+\alpha)^{-2}) \\ &\quad - (F(1+\alpha) - \beta F'(1+\alpha))(\alpha^{-1} + \beta\alpha^{-2})], \\ C_2 &= E[(F(\alpha) - \beta F'(\alpha))(1+\alpha-\beta) - (F(1+\alpha) - \beta F'(1+\alpha))(\alpha - \beta)], \end{aligned} \tag{12}$$

with $E = [(\alpha-\beta)((1+\alpha)^{-1} + \beta(1+\alpha)^{-2}) - (1+\alpha-\beta)(\alpha^{-1} + \beta\alpha^{-2})]^{-1}$. In the case of a uniform magnetic field when $f(r) = 1$, Eq. (11) reduces to the flat-film-limit velocity profile derived in Ref. [35].

C. Linear stability of the azimuthal flow

We consider azimuthally periodic perturbations of the base velocity and concentration fields in the form $(u', v', M_e^2 c') = (\tilde{u}(r), \tilde{v}(r), M_e^2 \tilde{c}(r))\mathrm{e}^{\lambda_n t + \mathrm{i}n\theta} + \text{c.c.}$, where c.c. denotes complex conjugate and $\lambda_n = \lambda_n^R + \mathrm{i}\lambda_n^I$ is the complex amplification rate of perturbations and n is the azimuthal wave number. Upon cancelling the common exponential factor the linearization of Eqs. (4)–(6) about the basic flow fields $(v_0, 1+M_e^2 c_0)$ leads to

$$\lambda_n \tilde{u} = \left[\frac{1}{\mathrm{Re}}\left(\frac{\mathrm{d}^2}{\mathrm{d}r^2} + \frac{1}{r}\frac{\mathrm{d}}{\mathrm{d}r} - \frac{1+n^2}{r^2}\right) - \frac{\mathrm{i}nv_0}{r}\right]\tilde{u} + \frac{2}{r}\left[v_0 - \frac{\mathrm{i}n}{\mathrm{Re}\, r}\right]\tilde{v} - \frac{\mathrm{d}c}{\mathrm{d}r}, \tag{13}$$

$$\lambda_n \tilde{v} = \left[\frac{2\mathrm{i}n}{\mathrm{Re}\, r^2} - \frac{\mathrm{d}v_0}{\mathrm{d}r} - \frac{v_0}{r}\right]\tilde{u} + \left[\frac{1}{\mathrm{Re}}\left(\frac{\mathrm{d}^2}{\mathrm{d}r^2} + \frac{1}{r}\frac{\mathrm{d}}{\mathrm{d}r} - \frac{1+n^2}{r^2}\right) - \frac{\mathrm{i}nv_0}{r}\right]\tilde{v} - \frac{\mathrm{i}nc}{r}, \tag{14}$$

$$0 = \left[\frac{\mathrm{d}}{\mathrm{d}r} + \frac{1}{r}\right]\tilde{u} + \frac{\mathrm{i}n}{r}\tilde{v}, \tag{15}$$

which is a generalized eigenvalue problem for λ_n. The perturbation velocity fields must satisfy the following boundary conditions:

$$\tilde{u} = 0 \ \text{ and } \ \tilde{v} = \beta\frac{\mathrm{d}\tilde{v}}{\mathrm{d}r} \text{ at } r = \alpha \text{ and } \ \tilde{v} = -\beta\frac{\mathrm{d}\tilde{v}}{\mathrm{d}r} \text{ at } r = 1+\alpha. \tag{16}$$

It is convenient to rewrite these equations in a perturbation energy form. To do that, we multiply Eqs. (13) and (14) by the complex conjugate eigenfunctions $\tilde{u}^*$ and $\tilde{v}^*$, respectively; add them together; multiply by r; and integrate over $\alpha \leqslant r \leqslant 1+\alpha$ (by parts where necessary), making use of the continuity equation (15) and boundary conditions (16). This results in the following (generally complex) equation:

$$\lambda_n \Sigma_k = \Sigma_a + \Sigma_c + \Sigma_s - 1, \tag{17}$$

where

$$\Sigma_{\{\cdot\}} = \frac{\int_\alpha^{1+\alpha} E_{\{\cdot\}}\,\mathrm{d}r}{\left|\int_\alpha^{1+\alpha} E_v\,\mathrm{d}r\right|}, \quad E_k = r(|\tilde{u}|^2 + |\tilde{v}|^2), \quad E_a = -\mathrm{i}nv_0(|\tilde{u}|^2 + |\tilde{v}|^2),$$

$$E_c = 2v_0\tilde{u}^*\tilde{v}, \quad E_s = -\frac{\mathrm{d}(rv_0)}{\mathrm{d}r}\tilde{u}\tilde{v}^*,$$

$$E_v = -\frac{1}{\mathrm{Re}}\left[r\left(\left|\frac{\mathrm{d}\tilde{u}}{\mathrm{d}r}\right|^2 + \left|\frac{\mathrm{d}\tilde{v}}{\mathrm{d}r}\right|^2\right) + \frac{n^2-3}{r}|\tilde{u}|^2 + \frac{n^2+1}{r}|\tilde{v}|^2 + \beta\left(\alpha\left(\left|\frac{\mathrm{d}\tilde{v}}{\mathrm{d}r}\right|_\alpha\right)^2 + (1+\alpha)\left(\left|\frac{\mathrm{d}\tilde{v}}{\mathrm{d}r}\right|_{1+\alpha}\right)^2\right)\right].$$

The term Σ_k is real and positively defined. It represents the kinetic energy of perturbations. Therefore, the sign of the perturbation growth rate λ_n^R and, consequently, the stability of base flow is determined by the sign of the sum of real parts of the terms on the right-hand side of Eq. (17). More specifically, the sign of individual terms determines whether they play stabilizing (if their real parts are negative) or destabilizing (if their real parts are positive) roles. The physical meaning of each of these terms is easily identifiable, offering a straightforward way of determining which physical mechanism is responsible for the onset of instability for a given set of the governing parameters. Namely, Σ_a characterizes azimuthal advection of perturbations. This term is imaginary and does not contribute to the instability onset or decay. The expression for E_a indicates that the sign of λ^I is opposite that of v_0. Therefore, upon writing the exponential term as $\mathrm{e}^{\mathrm{i}(\lambda^I t + n\theta)} = \mathrm{e}^{\mathrm{i}n(\theta - \omega_n t))}$ and recognizing that the angular translation speed $\omega_n = -\lambda_n^I/n \sim \frac{v_0}{r}$, we conclude that perturbations are essentially carried by the base flow and their propagation speed is close to that of the base flow at the location of the perturbation maximum. The complex-valued term Σ_c is related to the centrifugal term $-\frac{v^2}{r}$ in radial momentum equation (4), which disappears when $r \to \infty$, while Σ_s (also complex valued) is traced back to the flow shear. Finally, the term Σ_v quantifies viscous dissipation. It is real and negatively defined so that perturbation energy balance equation (17) is scaled with its magnitude. Therefore, the instability in the considered setup may be due to the action of either centrifugal or shear mechanisms.

Alternatively, the linear stability problem can be formulated in terms of the flow vorticity $\omega = \omega_0 + \tilde{\omega}(r)e^{\lambda_n t + in\theta}$ and the stream function $\psi = \psi_0 + \tilde{\psi}(r)e^{\lambda_n t + in\theta}$, where $\tilde{\omega}$ and $\tilde{\psi}$ denote the infinitesimal perturbations. Upon linearizing Eq. (8) we obtain the Orr-Sommerfeld equation for the perturbation of the stream function:

$$\tilde{\lambda}_n \nabla^2 \tilde{\psi} + W \frac{in}{r}\left[\frac{f(r)}{r} + g(r)\nabla^2\right]\tilde{\psi} = \nabla^4 \tilde{\psi}, \tag{18}$$

where $\nabla^2 = \partial_{rr} + r^{-1}\partial_r - n^2 r^{-2}$ and $W = \mathrm{Re}\ln(1+\alpha^{-1})^{-1}$ is the modified viscous Lorentz parameter, the function $g(r)$ is given by Eq. (11), and $\tilde{\lambda}_n = \tilde{\lambda}_n^R + i\tilde{\lambda}_n^I = \mathrm{Re}\lambda_n$ represents the scaled perturbation growth rate.

Therefore, for any given distribution of magnetic field $f(r)$, the stability of the nth azimuthal mode is determined by the solutions of eigenvalue problem (18). By requiring that the radial velocity u vanishes at $r = \alpha$ and $r = 1 + \alpha$ and applying Eq. (7), we obtain four boundary conditions,

$$\tilde{\psi} = 0, \quad \partial_r \tilde{\psi} = \pm\beta\partial_{rr}\tilde{\psi}, \tag{19}$$

where the plus and minus signs correspond to $r = \alpha$ and $r = 1 + \alpha$, respectively.

The analytic solution of Eq. (18) with no-slip boundaries in the absence of the Lorentz force, that is, when $W = 0$, was obtained in Ref. [6]. In the case of the slip boundaries, the solution is given in the Appendix. For each wave number $n = 1, 2, \ldots$, the spectrum of the eigenvalues is discrete: $\tilde{\lambda}_{nl} = \tilde{\lambda}_{nl}^R + i\tilde{\lambda}_{nl}^I$, $l = 0, 1, 2, \ldots$, where the index l sorts the modes in order of descending growth rate $\tilde{\lambda}_{nl}^R$ so that $l = 0$ corresponds to the least stable mode with a fixed wave number n. For a given magnetic field distribution $f(r)$, we use numerical continuation [39,40] to continue the mode nl in parameters W and/or α and β. The eigenfunctions $\tilde{\psi}$ are discretized using the orthogonal collocation method with four collocation points and up to 300 adaptively distributed points in each subinterval. This enables the effective resolution of rapid variations of solution, which is typical for boundary layers.

To obtain the loci of the neutral stability points (W, α) we proceed as follows. For every azimuthal number n we continue the least stable mode $l = 0$ starting with the analytically known solution at $W = 0$ and $\beta = 0$ and use W as the principal continuation parameter. Once the neutral stability point $\tilde{\lambda}_{n0}^R = 0$ is found, we continue the solution in α and/or β while keeping the real part of the eigenvalue fixed at $\tilde{\lambda}_{n0}^R = 0$. This enables us to obtain the loci of neutral points for the $l = 0$ mode with wave number n. We then repeat the procedure for up to four next least stable modes $l = 1, 2, 3, 4$. While doing so, we did not find neutrally stable modes with $l > 0$. Therefore, the base flow is found to be unstable with respect to at most one perturbation mode for each azimuthal wave number n.

IV. MARGINAL STABILITY OF THE BASE FLOW IN A UNIFORM MAGNETIC FIELD

We consider the case of no-slip boundary conditions and a uniform magnetic field with $f(r) = 1$ first. The neutral stability curves for the above flow profiles and the first ten azimuthal modes with wavenumbers $n = 2, \ldots, 10$ are shown in Fig. 1(a). The mode with $n = 1$ always decays. This is similar to the stability of a monopole vortex in inviscid fluid occupying unbounded space [3,13].

In the limit of large α the flow in an annulus approaches the plane Poiseuille flow. The well-known value of the critical Reynolds number based on the half-width of a channel and the maximum flow speed is $\mathrm{Re}_P \approx 5772.22$ [41]. The equivalent value of the Reynolds number based on the scales adopted here is $\mathrm{Re} = \frac{2\mathrm{Re}_P}{v_{\max}}$. In the limit of $\alpha \to \infty$ and for $\beta = 0$ the maximum of the azimuthal velocity given by Eq. (11) tends to $v_{\max} = \frac{1}{8}$ so that $\mathrm{Re} \to 16\mathrm{Re}_P$, which is shown by the dotted line in Fig. 1. The value of α for the smallest Re along the marginal stability curve in this limit then is determined from the condition that the instability wavelength in an annulus approaches that of

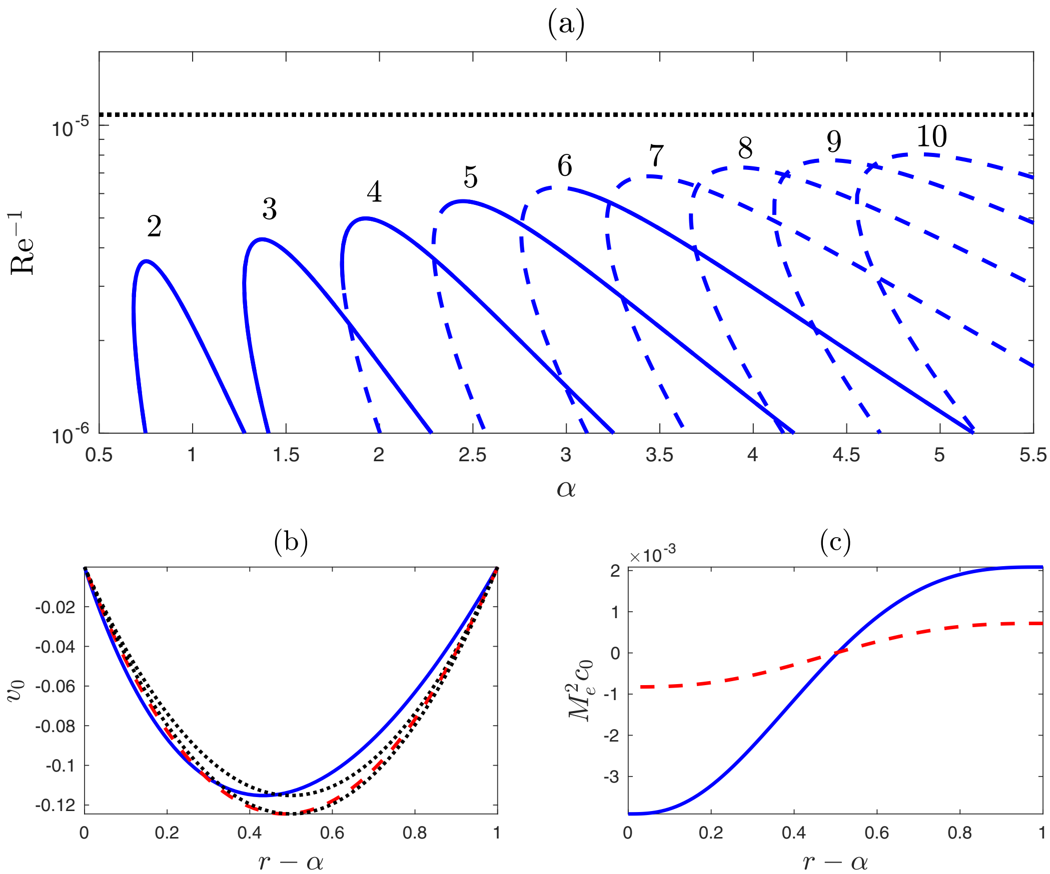

FIG. 1. (a) Neutral stability diagram of the base flow with no-slip boundary conditions in a uniform magnetic field with $f(r) = 1$. The flow is stable above the neutral stability curves. The numerical labels show the values of the azimuthal wave number n for each curve. The dotted horizontal line corresponds to the critical Reynolds number for plane Poiseuille flow. The solid and dashed segments of the neutral stability curves correspond to the centrifugal (curvature-related) and shear instability mechanisms, respectively. (b) Azimuthal velocity of the base flow for $(\alpha, \mathrm{Re}) = (0.752, 2.764 \times 10^5)$ (solid line) and $(\alpha, \mathrm{Re}) = (4.875, 1.241 \times 10^5)$ (dashed line) that correspond to the tips of the neutral instability tongues for $n = 2$ and $n = 10$, respectively, in a uniform magnetic field. The dotted lines show the corresponding velocity profiles for the plane Poiseuille flow. (c) Surfactant concentration for the same parameters as in panel (b).

plane Poiseuille flow:

$$\frac{2\pi r_1}{n} \to \frac{2\pi(r_2 - r_1)}{2\gamma_P},$$

where $\gamma_P \approx 1.02$ (e.g., Ref. [41]) is the critical nondimensional wave number of plane Poiseiulle flow (scaled with the half-width of the channel). That is, $\alpha_c \approx \frac{n}{2\gamma_P} \approx \frac{n}{2}$ as indeed is seen in Fig. 1 for large n.

The velocity of the base azimuthal flow and the steady surfactant concentration for small and large annulus radii are shown in Figs. 1(b) and 1(c). The selected values of α and Re correspond to the upper tips of the neutral stability tongues with $n = 2$ and $n = 10$. As the radius increases, the velocity profile approaches that of plane Poiseuille flow [compare the solid and dashed lines in Fig. 1(b)], and the radial concentration gradient (playing the role of the pressure gradient) decreases

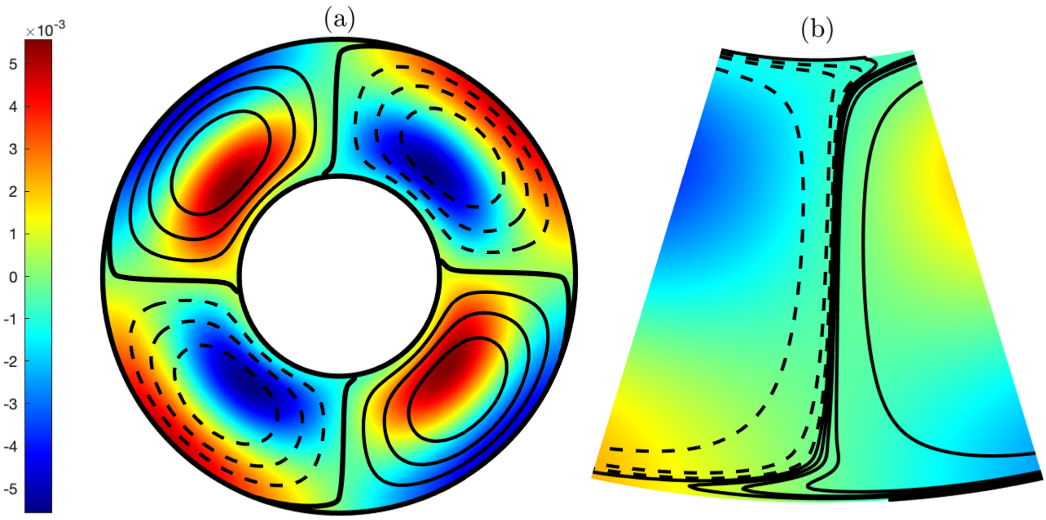

FIG. 2. (a) Instantaneous disturbance streamlines for the neutral mode with $n = 2$ at the critical point $(\alpha, \mathrm{Re}) = (0.762, 2.764 \times 10^5)$. The streamlines of anticlockwise and clockwise rotations are shown by solid and dashed lines, respectively. The complete pattern is carried by the annular base flow clockwise. The color represents the perturbation of a surfactant field $\Re\{\tilde{c}e^{in\theta}\}$ (arbitrary scale). (b) Close-up of streamlines near the boundary of neighboring vortices and the no-slip walls.

(it is identically zero in the plane Poiseuille flow) [see Fig. 1(c)]. The perturbation streamlines for the critical disturbance mode with wave number $n = 2$ are shown in Fig. 2(a). This mode consists of $n = 2$ pairs of counterrotating vortices (the azimuthal wave number can be interpreted as the number of vortex pairs present in the perturbation field). The regions of high surfactant concentration (that plays the role of pressure) are located near the outer cylinder for cyclonic vortices (vortices that rotate in the same sense as the base flow) and near the inner cylinder for their anticyclonic counterparts.

The close-up of a region near the boundary separating two counterrotating vortices is shown in Fig. 2(b). It reveals that a very thin zone (about 1% of the annulus width) exists in the regions, where the separatrix streamline approaches the solid walls and where the azimuthal perturbation velocity component reverses its direction. Typical distributions of perturbation energy balance integrands (17) shown in representative Figs. 3 and 4 enable us to identify the physical nature of instability as centrifugal and shear, respectively. Specifically, from Figs. 3(a) and 4(a), we see that most of the perturbation kinetic energy is concentrated near the no-slip boundaries. However, the detailed distribution of physical mechanisms responsible for its generation are qualitatively different for flows in annuli of small and large radii. In Fig. 3, the curvature-related (centrifugal) disturbances [the dashed line in Fig. 3(b)] dominate near the inner cylinder, where the curvature is larger. Flow shear still destabilizes the flow locally near the outer cylinder. However, flow shear plays a strongly stabilizing role near the inner cylinder so that overall it leads to flow stabilization for small α. The viscous dissipation only plays a significant role near the no-slip boundaries.

At larger radii the base flow approaches its plane Poiseuille counterpart [see Fig. 1(b)] and the perturbation energy production becomes more symmetrically distributed between the boundary layers at the inner and outer cylindrical walls [see the dash-dotted line in Fig. 4(b)]. The curvature effects [the dashed line in Fig. 4(b)] play almost no role in triggering instability at large α and it takes the form of the well-studied Tollmien-Schlichting waves [42].

The transition between the two types of instabilities occurs in a continuous way as illustrated in Fig. 1: low-Reynolds-number and/or small-radius regimes are dominated by curvature effects ($\Sigma_c^R > \Sigma_s^R$) while shear plays the major destabilizing role ($\Sigma_s^R > \Sigma_c^R$) in fast small-curvature flows.

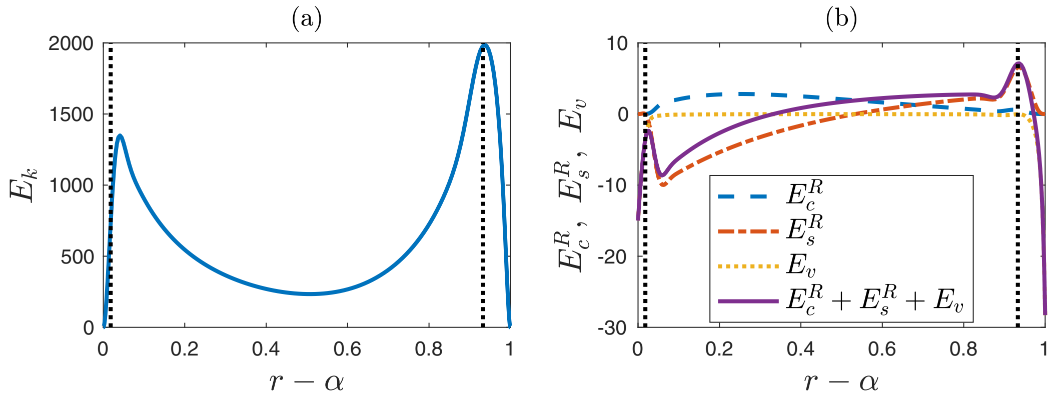

FIG. 3. Perturbation energy integrands for the neutral mode with $n = 2$ at the critical point $(\alpha, \mathrm{Re}) = (0.752, 2.764 \times 10^5)$. The vertical dotted lines show the locations of the critical layers, where the translation speed $-\frac{\lambda^I r}{n}$ of instability patterns is equal to the local azimuthal base flow speed $v_0(r)$. Centrifugal (curvature-related) instability: $\Sigma_c^R = 3.256$, $\Sigma_s^R = -2.256$.

For all α the maxima of the perturbation energy production are located in close proximity of critical layers, where the propagation speed of perturbations is equal to that of the local base flow (see the vertical dotted lines in Figs. 3 and 4).

Slip length influence on the flow stability

The stability of the base flow in a uniform magnetic field is highly sensitive to the boundary conditions at the film edges. Figure 5(a) demonstrates how the stability threshold in the plane $(\mathrm{Re}^{-1}, \alpha)$ for the second and the third azimuthal modes changes with the slip length. The critical values of Re for the onset of instability increase with β and so do the values of α at which the instability establishes. Figure 5(b) shows the value of Re^{-1} that corresponds to the neutral stability boundary as a function of β for fixed n and α. The stabilizing effect of the slip length was earlier reported for the plane Poiseuille flow in Ref. [43]. It is associated with the reduction of boundary layer shear in slip flows.

To better understand the influence of the slip length on the flow stability, we computed the neutral stability curves for the case of mixed boundaries, imposing the no-slip condition at the inner cylinder

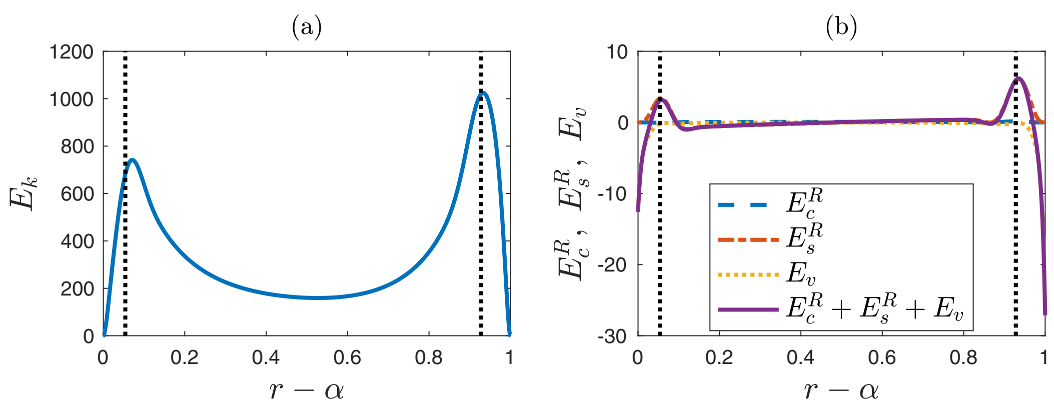

FIG. 4. Same as Fig. 3 but for $n = 10$ and $(\alpha, \mathrm{Re}) = (4.875, 1.241 \times 10^5)$. Boundary layer (shear) instability (Tollmien-Schlichting waves): $\Sigma_c^R = 0.099$, $\Sigma_s^R = 0.901$.

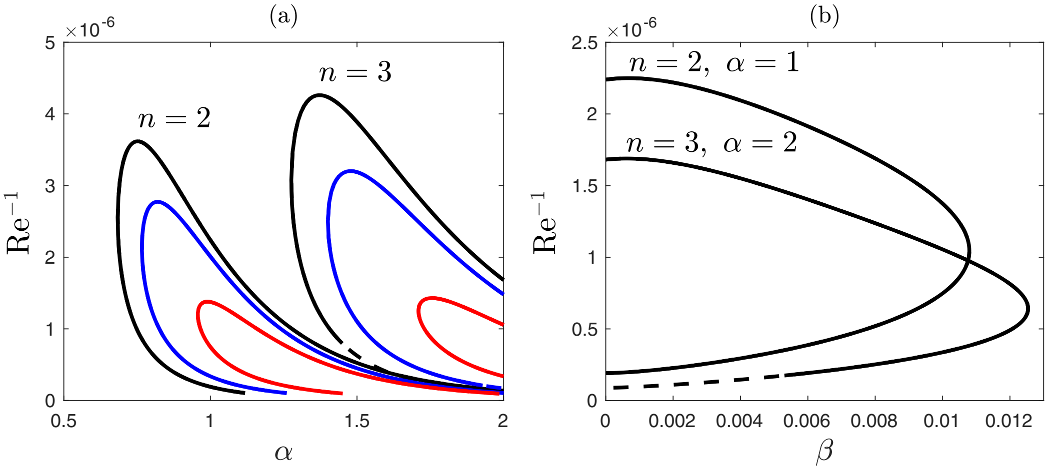

FIG. 5. Influence of the slip length β on the stability of the base flow in a uniform magnetic field. Neutral stability curves (a) for $\beta = 0$ (black), $\beta = 0.005$ (blue), $\beta = 0.010$ (red), and azimuthal wavenumbers $n = 2$ and 3; (b) for fixed $(n, \alpha) = (2, 1)$ and $(n, \alpha) = (3, 2)$. The solid and dashed segments of the neutral stability curves correspond to the centrifugal (curvature-related) and shear instability mechanisms, respectively.

and assuming a partial slip on its outer counterpart (not presented here). We found a trend similar to that illustrated in Fig. 5(a). Namely, as β increases, the base flow velocity gradient in the flow domain decreases, and the flow approaches a plug type, which is known to be stable. Subsequently, the neutral stability curve is pushed toward larger values of Re. In the perfect-slip limit at the outer cylinder, the base flow was found to be linearly stable for perturbations with all azimuthal wave numbers n. This confirms that the existence of a sufficiently strong velocity inhomogeneity in the flow domain is the necessary condition for the onset of instability.

V. FLOW STABILITY AND FINITE-AMPLITUDE VORTICES IN A PIECEWISE-CONSTANT MAGNETIC FIELD

It is known that a parallel flow with strong velocity shear (e.g., Kolmogorov flow) is susceptible to instabilities. The linear stability of an axisymmetric base flow with the azimuthal velocity given by the Bessel function $J_1(r)$ was studied earlier [6]. However, creating such a flow in practice is problematic as it would require a sophisticated array of magnets to produce the desired dependence of the Lorentz force on the radial coordinate. On the other hand, an approximately piecewise-constant field with a constant intensity B_1 in the region $r_1 < r < r_m$ and some other constant intensity B_2 in $r_m < r < r_2$ is relatively easy to realize by inserting a cylindrical magnet with the outer radius r_m into another ring magnet with the inner radius r_m and the opposite polarity. In this configuration, assuming that the two magnets have equal magnetization, the function $f(r)$ is given by $f(r) = \pm 1$ for $r \gtrless r_m$. To avoid dealing with jump discontinuities, we approximate $f(r)$ with

$$f(r) = \tanh\left(s\left(r - \tfrac{1}{2} - \alpha\right)\right), \tag{20}$$

where we assume that the jump occurs in the middle of the gap between two electrodes and introduce the parameter s that controls the steepness of the jump ($s = 20$ in computations reported below).

The representative base flow profiles and the steady distribution of surfactant for such a piecewise-constant magnetic field are shown in Figs. 6(a) and 6(b) for various values of the slip length. For the chosen magnetic field distribution the base flow is clockwise near the outer cylinder and anticlockwise in the inner region for all slip length values. However, the dependence of the shape of the velocity profile on β is not monotonic. For no-slip boundaries the maximum of the

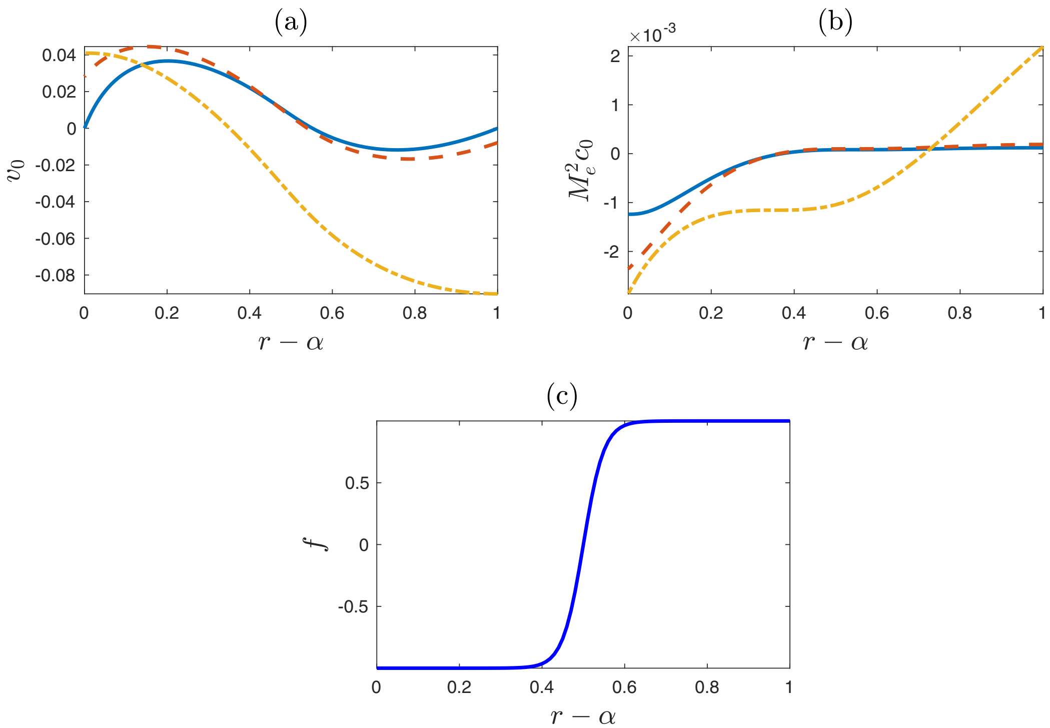

FIG. 6. Representative base flow profiles for $(\alpha, \mathrm{Re}) = (0.1, 2000)$ and $\beta = 0$ (solid lines), $\beta = 0.1$ (dashed lines), and $\beta \to \infty$ (dash-dotted lines) in piecewise-constant magnetic field (20) shown in (c): (a) azimuthal velocity and (b) surfactant concentration.

azimuthal velocity is located near the inner cylinder and initially it grows with β when it is small [see the solid and dashed lines in Fig. 6(a)]. However, if the slip length increases beyond a certain value, the growth of the azimuthal velocity maximum near the inner cylinder is hindered and the velocity magnitude near the outer cylinder starts to increase [see the dash-dotted line in Fig. 6(a)]. This has an impact on the propagation direction of the instability vortices (more details are given below).

The stability diagram of the base flow in the piecewise-constant field for no-slip boundaries is shown in Fig. 7(a) for the azimuthal modes with wave number $n = 1$–8. The neutral stability curve for the mode with wave number $n = 1$ lies in the region where modes with larger wave numbers have a positive growth rate. For example, at $\alpha = 0.1$, the basic flow becomes unstable with respect to the $n = 2$ mode at a smaller value of the Reynolds number than that for $n = 1$. The azimuthal wave number of the most dangerous instability mode progressively increases with α so that the number of vortex pairs becomes larger.

Figures 7(b) and 7(c) demonstrate the variation of stability properties of the flow as the slip length increases. Several trends are visible. As the degree of slip increases, the instability sets in at progressively smaller Reynolds number. This is related to the reduction of viscous dissipation near the solid walls. As the value of β increases, the neutral stability curves corresponding to $n > 1$ shift toward the larger values of α. That is, the onset of the corresponding instabilities requires a channel with a smaller curvature. The instability mode with $n = 1$ behaves in a qualitatively different way. The shift of its critical point toward the larger radii is not as strongly pronounced while its translation to smaller values of the Reynolds number happens faster than for modes with larger wave numbers so that it becomes dominant in high-slip flows [see Fig. 7(c)]. These observations are indicative of the fact that the $n = 1$ and $n > 1$ instability modes illustrated in Figs. 8(a) and 8(b)

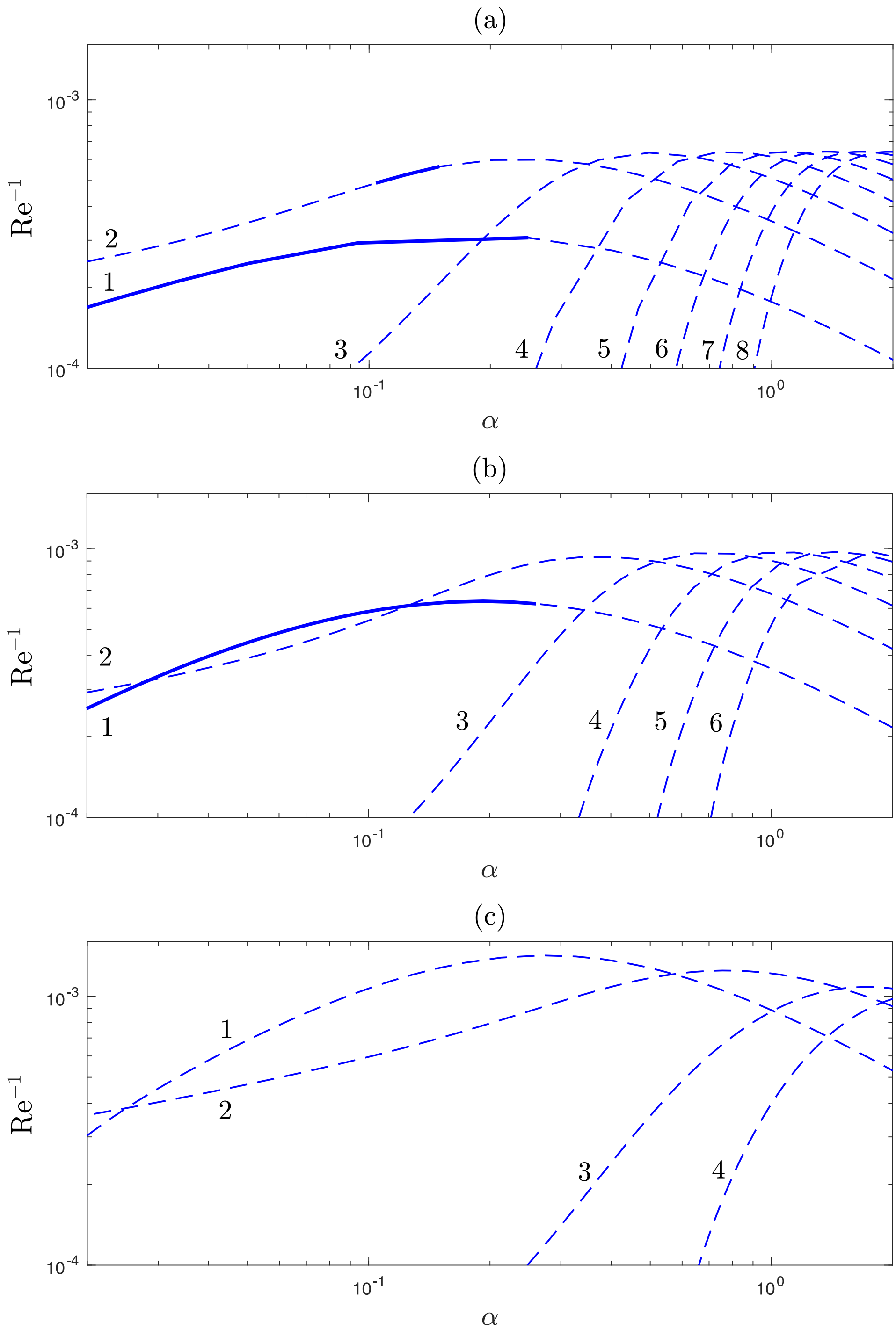

FIG. 7. Stability diagrams for the base flow with (a) no slip, (b) partial slip with $\beta = 0.1$, and (c) full slip $\beta \to \infty$ boundaries in a piecewise-constant magnetic field $f(r) = \tanh(20(r - \frac{1}{2} - \alpha))$. The solid and dashed segments of the neutral stability curves correspond to the centrifugal (curvature-related) and shear (inviscid inflection point) instability mechanisms, respectively. The numerical labels indicate the azimuthal wave numbers n.

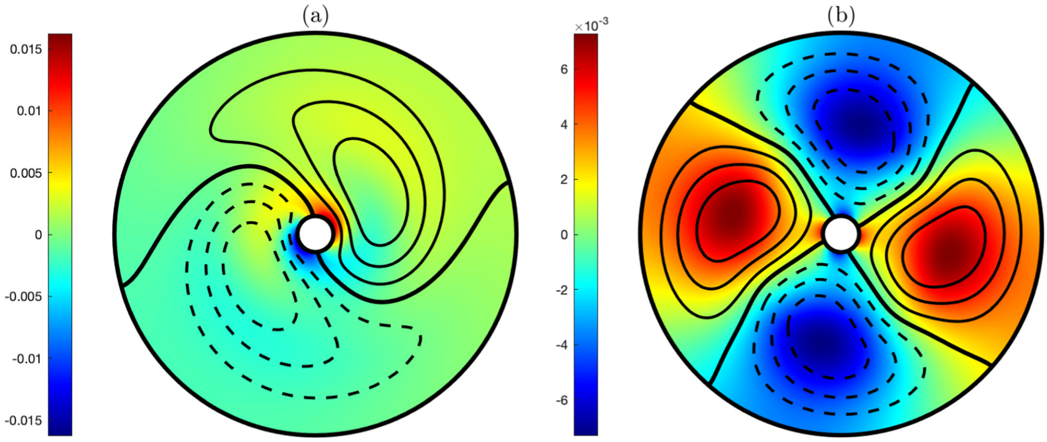

FIG. 8. Instantaneous disturbance streamlines for the neutral mode with (a) $n = 1$ at $(\alpha, \mathrm{Re}) = (0.1, 1.720 \times 10^3)$ precessing clockwise and (b) $n = 2$ at $(\alpha, \mathrm{Re}) = (0.1, 1.860 \times 10^3)$ propagating anticlockwise. The streamlines of anticlockwise and clockwise rotations are shown by solid and dashed lines, respectively. The color represents the perturbation of a surfactant field $\Re\{\tilde{c}e^{in\theta}\}$ (arbitrary scale).

may have a different physical nature. Indeed, the visual difference between these two modes is not limited to only the total number of the present vortex pairs. The $n = 1$ and $n > 1$ modes precess (drift) in the opposite directions: the former always follows the base flow motion near the outer cylinder (clockwise) while the latter precesses in the direction of the base flow in the inner region (anticlockwise) for no- or small-slip boundaries (solid and dashed profiles in Fig. 6) or near the outer cylinder (clockwise) for strong slip (dash-dotted profiles in Fig. 6). Furthermore, the $n = 1$ mode is characterized by much more uniform surfactant distribution with most of its variation occurring close to the inner cylinder. In contrast, in $n > 1$ modes the largest variation of surfactant is away from the boundaries, suggesting that the highest-intensity perturbations are not associated with the proximity to the solid walls.

To pinpoint the physical destabilization mechanisms for the two types of instability modes, we present in Figs. 9 and 10 and compare perturbation energy integrands (17) for the $n = 1$ and $n = 2$ modes at their respective neutral stability points. Figure 9(b) demonstrates that the majority of the perturbation energy production for the mode with wave number $n = 1$ is due to the curvature (centrifugal effects) with flow shear contributing significantly less. As seen from Fig. 9(a) the most energetic perturbations are localized near the inner cylinder (the high-curvature region), where they indeed are expected to experience the strongest centrifugal push. We also note that the radial locations where the perturbation precession velocity of the $n = 1$ mode is equal to the local basic flow speed shown by the vertical dotted lines do not correlate with the maximum of perturbation energy production. This is in striking contrast with the energy production for the $n = 2$ mode shown in Fig. 10(b). There the peak of energy production coincides with the location of the critical layer that in turn coincides with the location of the inflection point (maximum shear point) of the base flow velocity profile. Thus, we conclude that the differences in the behavior of the $n = 1$ and $n > 1$ modes are explained by the fact that they are triggered by two completely different physical mechanisms: curvature-related centrifugal effects in the first case and classical inflection point shear instability [42] in the second. Consequently, while shear instability is expected to be robust, the centrifugal instability would disappear in annuli of large radii when the curvature effects become small. This is indeed confirmed by our computations summarized in Fig. 7: even for the $n = 1$ mode the centrifugal influence reduces and is eventually superseded by shear destabilization as α increases.

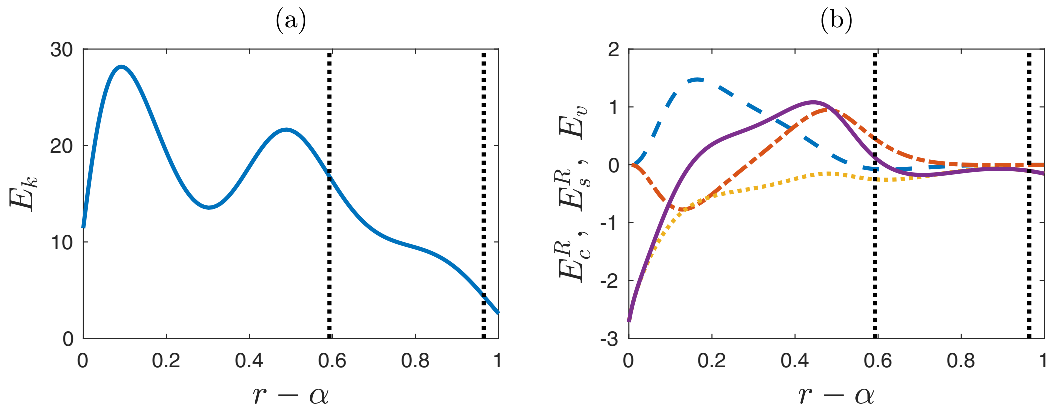

FIG. 9. Perturbation energy integrands for the neutral mode with $n = 1$ at the point $(\alpha, \mathrm{Re}) = (0.1, 1.720 \times 10^3)$. The vertical dotted lines show the locations where the translation speed $-\frac{\lambda^I r}{n}$ of instability patterns is equal to the local azimuthal base flow speed $v_0(r)$. Centrifugal (curvature-related) instability: $\Sigma_c^R = 0.806$, $\Sigma_s^R = 0.194$. (b) The dashed line represents E_c^R, the dashed-dotted line E_s^R, the dotted line E_v, and the solid line $E_c^R + E_s^R + E_v$.

Onset of vortices and their temporal evolution

In Fig. 11 we present the nonlinear time evolution of the developing instability obtained by numerically solving Navier-Stokes equations (4) and (5) with no-slip boundary conditions using a simple nonincremental pressure correction scheme [44]. The electric potential difference is abruptly applied when the fluid is at rest. We choose Re = 2500, which corresponds to a linearly unstable base flow [refer to Fig. 1(a)]. The initial conditions correspond to the base azimuthal flow with the superposed uniformly distributed noise with amplitude 10^{-3}.

Until $t \approx 900$, the flow is predominantly azimuthal with the largest speed attained in the inner part of the annulus ($\alpha < r < \alpha + \frac{1}{2}$), where fluid rotates anticlockwise. In the outer region ($\alpha + \frac{1}{2} < r < \alpha + 1$), the flow is clockwise. For $\alpha = 0.1$ (the top row in Fig. 11), two vortices appear at $t \approx 1200$ with their centers located diametrically opposite to each other. For $\alpha = 0.5$ (the middle row in Fig. 11) and $\alpha = 0.8$ (the bottom row in Fig. 11), three and four stable vortices are found,

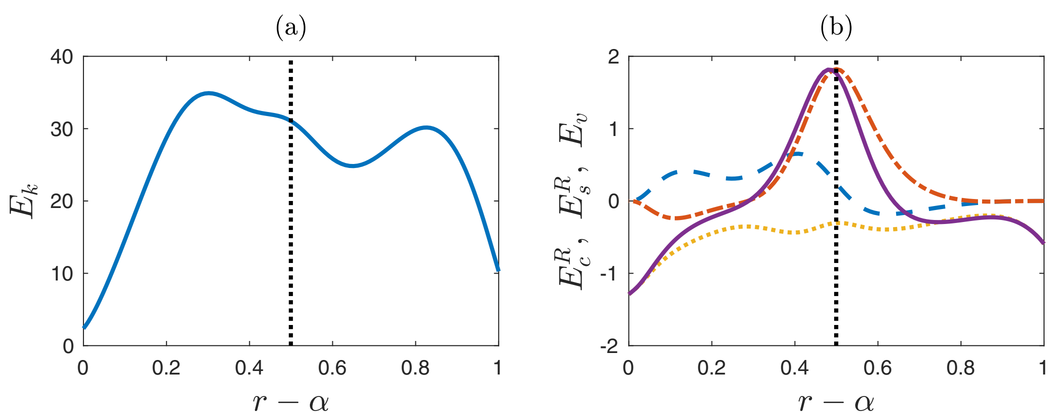

FIG. 10. Same as Fig. 9 but for $n = 2$ and $(\alpha, \mathrm{Re}) = (0.1, 1.860 \times 10^3)$. Inflection point (shear) instability: $\Sigma_c^R = 0.325$, $\Sigma_s^R = 0.675$. (b) The dashed line represents E_c^R, the dashed-dotted line E_s^R, the dotted line E_v, and the solid line $E_c^R + E_s^R + E_v$.

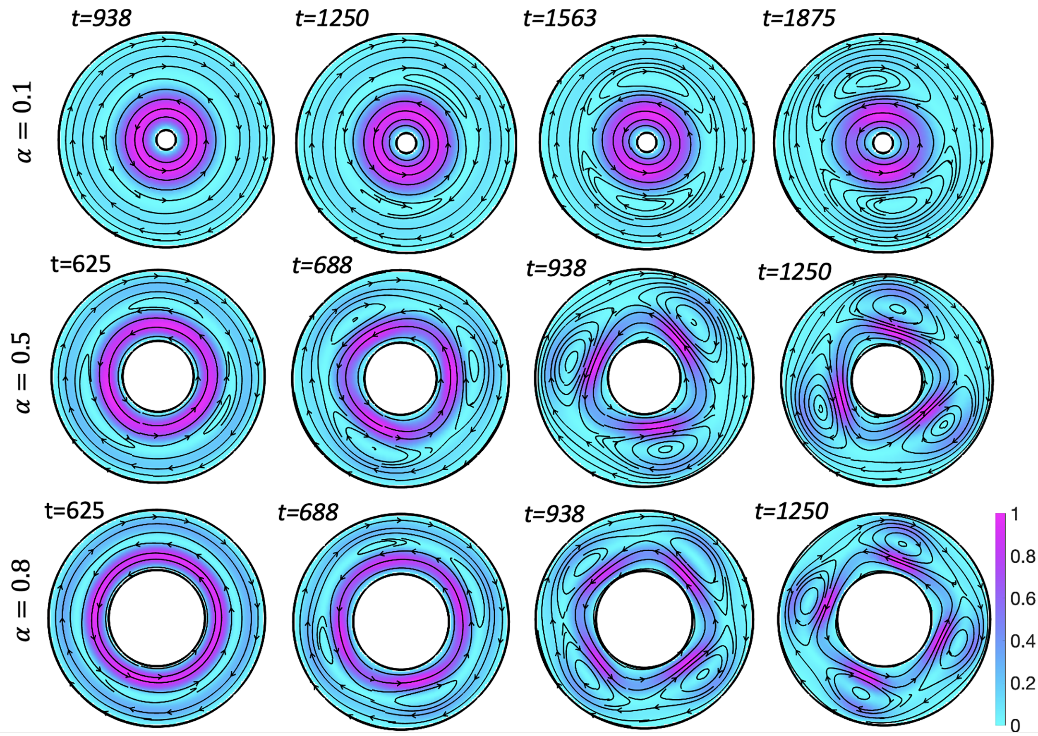

FIG. 11. Temporal evolution (instantaneous streamlines) of the film flow with no-slip boundaries for $\mathrm{Re} = 2500$ in a piecewise-constant magnetic field for $\alpha = 0.1, 0.5,$ and 0.8. Initially, the fluid is at rest and the electric potential difference is applied at $t = 0$. Light and dark shades (light blue and purple online) show regions of low and high kinetic energy density $v^2 + u^2$, respectively.

respectively. In each case, the vortices slowly drift anticlockwise. The angular speed of the slow vortex drift decreases with α and vanishes when $\alpha \to \infty$ (symmetric inflection point instability limit). The computed vortices rotate clockwise and drift anticlockwise so that they can be regarded as anticyclones. However, the direction of the vortex drift and, therefore, the vortex polarity may vary with the Reynolds number (not shown).

The results of direct numerical simulations shown in Fig. 11 are in excellent agreement with those of the linear stability analysis presented in Fig. 7(a). Namely, according to Fig. 7(a), for $\alpha = 0.1$, the primary instability pattern consists of a vortex pair with the azimuthal wave number $n = 2$ at the critical Reynolds number of $\mathrm{Re} \approx 2080$. The resulting vortex flow field in the vicinity of the neutral stability boundary can be approximated as $\boldsymbol{u} = v_0\boldsymbol{e}_\theta + A\boldsymbol{u}_n$, where $v_0\boldsymbol{e}_\theta$ is the base flow field, $\boldsymbol{u}_n$ is the flow field of the leading instability mode with $n = 2$, which is shown in Fig. 8(b), and $A \ll 1$ is a small amplitude. The instability mode $\boldsymbol{u}_n$ is normalized so that $\int_\alpha^{1+\alpha} ru\,\mathrm{d}r = 1$. The streamlines of the so-reconstructed flow field are shown in Figs. 12(a) and 12(b) for $A = 0.001$ and $A = 0.005$, respectively. Upon comparing these fields with the upper row in Fig. 11, we find them almost identical. This indicates the absence of any secondary bifurcations of the flow fields in Fig. 11. In other words, the solutions in Fig. 11 likely result from the primary bifurcation (sub- or supercritical) of the base flow.

Similarly, we verify that the flow field patterns of the final long-time flow states for $\alpha = 0.5$ and $\alpha = 0.8$ in Fig. 11 are topologically equivalent to $\boldsymbol{u} = v_0\boldsymbol{e}_\theta + A\boldsymbol{u}_n$, where $n = 3$ for $\alpha = 0.5$ and $n = 4$ for $\alpha = 0.8$.

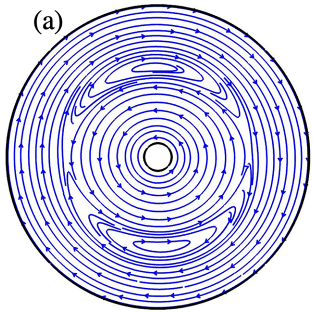

FIG. 12. Streamlines of the reconstructed flow field $\boldsymbol{u} = v_0\boldsymbol{e}_\theta + A\boldsymbol{u}_n$, where $v_0\boldsymbol{e}_\theta$ is the base flow at $\alpha = 0.1$ and Re $= 2080$ and $\boldsymbol{u}_n$ is the flow field of the leading instability mode with $n = 2$ from Fig. 8(b) for (a) $A = 0.001$ and (b) $A = 0.005$.

VI. EXPERIMENTS

We now investigate the existence of large-scale vortices in an electromagnetically driven flow in a soap film placed in a piecewise-constant magnetic field experimentally. The experiments were carried out in the configuration shown in Fig. 13. The radii of the outer and inner copper cylinders were $r_2 = 38$ and $r_1 = 10.5$ mm, respectively, corresponding to $\alpha = 0.38$. The height of the electrodes was 3 mm. An electrically conducting water-based mixture containing 12% soap (Axion), 15% NaCl, and 3% glycerine was used to create the film. The mass density, the dynamic viscosity, the surface tension, and the electrical conductivity of the working fluid were $\rho = 1100\ \mathrm{kg\,m^{-3}}$, $\mu = 1.5 \times 10^{-3}$ Pa s, $\sigma_s = 5.5 \times 10^{-2}\ \mathrm{N\,m^{-1}}$, and $\sigma = 5.9\ \mathrm{S\,m^{-1}}$, respectively. The initial thickness of the film was estimated to be $w_h = 1.5 \times 10^{-3}$ mm [45]. Experiments were conducted at 20°C. The cylindrical electrodes were embedded in a hollowed acrylic base placed on top of two ceramic ring magnets with outer diameters of 44.5 and 100 mm, inner diameters of 22 and 60 mm, and heights of 12.7 and 20 mm, respectively. The ring magnets were arranged concentrically with opposite polarities so that a distribution close to a piecewise-constant magnetic field was obtained. Note that there was a 7.75-mm gap between the inner and outer ring magnets so that a smooth transition existed between regions with counterdirected magnetic fields. The soap

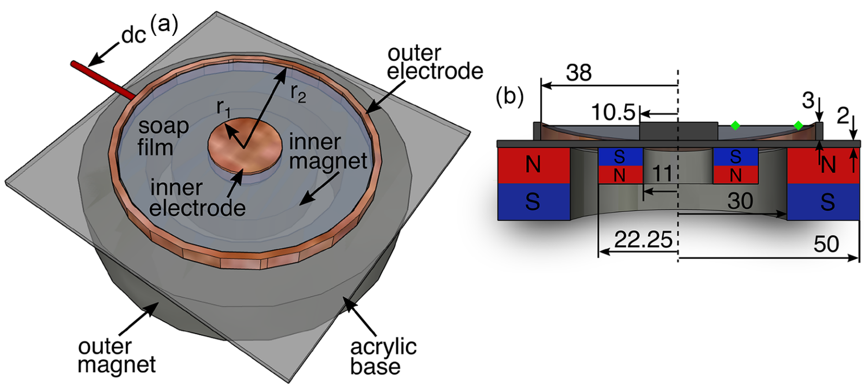

FIG. 13. Sketch of the experimental setup (not to scale): (a) isometric and (b) side views (dimensions are given in millimeters). A soap film spans the gap between two copper concentric cylindrical electrodes with radii r_1 and r_2. The electrodes are embedded in an acrylic base placed on top of two ceramic ring magnets with the opposite polarities. An electric potential difference is applied between the electrodes using a direct current power source.

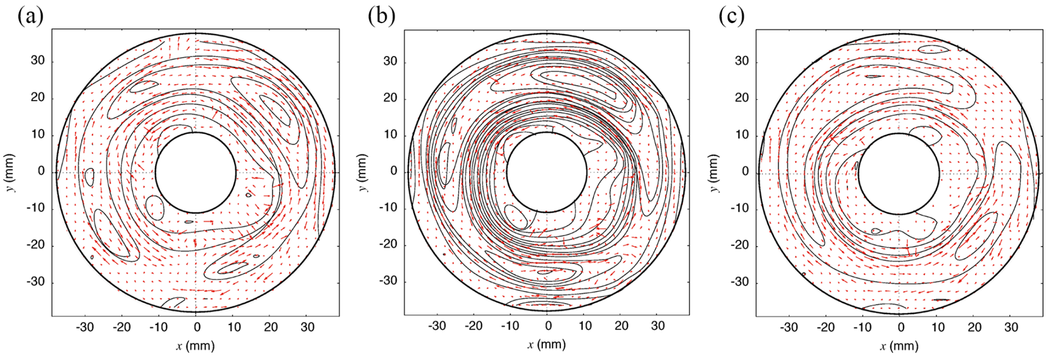

FIG. 14. Velocity fields and instantaneous streamlines of experimentally observed film flows obtained using particle image velocimetry: (a) four, (b) three, and (c) two vortices.

film was 5 mm above the magnets. The maximum magnetic field intensities measured with a tesla meter (model F.W. Bell 048) at the mid-radii of the inner and outer magnet rings at the height of the film [see the green markers in Fig. 13(b)] were -0.06 and 0.05 T, respectively. The ring electrodes were connected to a DC power source (Tektronix PS280) that supplied the radial electric current to the film. For currents in the range between 50 and 150 mA, azimuthal clockwise and anticlockwise flows were observed in the outer and inner regions, respectively. To observe the vortex formation the current was increased up to its maximum possible value of 300 mA limited by a (constant) 30 V output of the used power supply. However, after starting the experiment at such a limit it was observed that the current flowing through the film would uncontrollably decrease to 100 mA after approximately 15 s. According to Ohm's law, such a variation of an electric current was attributed to an increase of the electrical resistance of the film. Several factors have likely contributed to it. First, the thinning of the film due to its evaporation and the border suction effect leads to the reduction of the film's cross-section area and proportional increase of the ohmic resistance. Second, with the initial current of 300 mA at the applied potential difference of 30 V, Joule heating of 9 W is delivered to the film, which can cause a substantial increase in its temperature and, consequently, resistance. These factors severely limited the experimental observation time interval.

Experimental velocity fields were obtained using particle image velocimetry (PIV), and computed using the PIVLab toolbox [46]. Spherical glass particles with 10 μm diameter were used as tracers for the PIV measurements. Video recordings were captured using a Nikon D80 camera held 30 cm over the film with an AF Micro-Nikkor 60 mm *f*/2.8 lens. The velocity vector fields and the instantaneous streamlines from PIV are shown in Fig. 14. Three instability flow patterns were observed in a single experimental run: four vortices at $t \approx 3$ s [Fig. 14(a)], three vortices at $t \approx 4$ s [Fig. 14(b)], and two vortices at $t \approx 5$ s [Fig. 14(c)]. The variation of the number of the observed vortices is attributed to the time dependence of the electrical resistance of the soap film that caused a quick decrease of the electric current and, consequently, of the Lorentz forcing. The maximum amplitudes of the experimental velocity for the flow patterns in Figs. 14(a), 14(b), and 14(c) were $U_{\max} \approx 0.04$, 0.035, and 0.03 m s^{-1}, respectively. Therefore, the corresponding Reynolds numbers, $\mathrm{Re} = \frac{\rho U_{\max} L}{\mu}$, based on the width $L = r_2 - r_1$ of the gap between the cylinders were around 800, 700, and 600.

The intense Joule heating associated with a high electric current required to observe the instability patterns seems to be the main cause of the time dependence of the electrical resistance. In future experiments this effect could be moderated by reducing the applied current while using stronger magnets with a larger diameter.

VII. DISCUSSION AND CONCLUSIONS

The linear stability of the azimuthal flow occurring in a flat horizontal electromagnetically driven free film spanning the gap between two cylindrical electrodes has been investigated in the cases of uniform and piecewise-constant Lorentz forcing. Neglecting the drainage of the fluid from the flat film into the border region under the meniscus, we consider no-slip and partial-Navier-slip conditions for the tangential velocity at the edges of the film. The slip length parameter $\beta > 0$ accounts for an effective hydrodynamic lubrication effect of the meniscus allowing the fluid in the flat portion of the film to slip near the electrodes. The limit of $\beta \to 0$ recovers the standard Reynolds model of hydrodynamic lubrication with no-slip boundaries.

In the case of a uniform magnetic field and no-slip boundaries, the base azimuthal flow is unidirectional. Its velocity vanishes at the boundaries and reaches a maximum at the location that depends on the ratio of the radii $\frac{\alpha}{1+\alpha}$. While the limit of a zero inner radius is not accessible in this model due to constraints on the electric potential, our results show that the base flow remains linearly stable for any $\alpha < 0.69$, that is, for a radii ratio smaller than 0.4. In the opposite limit of large radii, $\alpha \to \infty$, the flow approaches a plane Poiseuille flow, which is known to become linearly unstable for Reynolds numbers larger than $\mathrm{Re}_P = \frac{\rho u_{\max} L}{2\mu} = 5772.22$, where $u_{\max}$ is the maximum flow velocity and L is the width of the channel. If the flow is driven by the Lorentz force, then the critical value of the potential difference applied between the electrodes that leads to instability in the large radii limit is $V \approx 16\mathrm{Re}_P \frac{\mu^2}{\sigma B_0 L^2 \rho}$. For any finite α, the base flow is more stable than the plane Poiseuille flow.

We found that the base flow between the no-slip boundaries in a uniform magnetic field is linearly stable with respect to a perturbation mode with the azimuthal wave number $n = 1$ for all considered Reynolds numbers. As the inner radius increases, the first mode that becomes unstable at $\alpha = 0.69$ and $\mathrm{Re} \approx 3.8 \times 10^5$ has wave number $n = 2$. This mode corresponds to the formation of two diametrically opposite vortices that drift in the direction of the base flow. The critical Reynolds number of this mode at $\alpha = 0.69$ is approximately four times larger than that for the plane Poiseuille flow. As α increases further, the dominant linear instability mode shifts toward larger values of n so that the number of observable vortices at the onset of the instability increases.

In the uniform magnetic field, the stability of the base flow is highly sensitive to the variations of the slip length β. For any given α, the instability can be completely suppressed if β is increased above a certain value. For example, for $\alpha = 1$, the base flow stabilizes if $\beta > 0.01$, that is, if the slip length is larger than about 1% of the width of the film. Because of that an experimental detection of the instability in a uniform magnetic field may be difficult or even impossible, due to an effective slip at the boundaries introduced by a meniscus.

In the case of a piecewise-constant field, the base flow rotates in the opposite directions at the inner and outer halves of the gap between the electrodes. The resulting reversing velocity profile contains an inflection point, where a shear instability sets at much smaller Reynolds numbers than those for the uniform magnetic field. Contrary to the case of a uniform magnetic field, the base flow can become unstable for any radii ratio. The dominant instability mode at small $\alpha \sim 10^{-1}$ has the wave number $n = 2$ in the case of no-slip boundaries and $n = 1$ for the perfect-slip boundaries. For intermediate values of α, the critical Reynolds number depends on the slip length only weakly, which makes the piecewise-constant-field setup a convenient choice for experimental observations of instability.

We have further determined that instabilities are caused by two physically distinct mechanisms: centrifugal (curvature-related) and shear with shear instability further splitting into two subclasses. The centrifugal instability occurs only in annuli with a sufficiently large curvature (small inner radius). It is present in both unidirectional (uniform magnetic field) and reversing (piecewise–constant magnetic field) base flows but it is more pronounced in the case of no-slip boundaries. In small-curvature annuli placed in a uniform magnetic field, the base flow between the no-slip boundaries approaches the plane Poiseuille flow. The main instability mechanism in this limit is a boundary-layer shear (Tollmien-Schlichting waves). Imposing the partialslip conditions, in this case, reduces it so that a complete stabilization of unidirectional base flow is observed as the slip length increases beyond a certain critical value. In contrast, increasing the degree of the boundary slip in the reversing base flow destabilizes- it. This effect is traced back to the fact that the application of a piecewiseconstant magnetic field leads to the formation of a shear zone in the middle of an annulus. Thus, we have shown that the instability in this case is of the inflection-point type. It sets when the shear rate of the flow exceeds the critical value proportional to the radial gradient of the azimuthal velocity, which increases when the boundary slip is allowed.

Both subtypes of shear instability are characterized by the maximum of perturbation energy production in the critical layers, where the perturbation wave speed is equal to the local base flow speed. As a result, shear instability structures are effectively advected by the local flow. In contrast, the precession direction of the centrifugal instability is not correlated to the local flow velocity and can be opposite to it.

Direct numerical simulations of the Navier-Stokes equations for a piecewise-constant magnetic field and no-slip boundaries shed light onto the temporal evolution of vortices in nonlinear regimes. For the near-critical Reynolds numbers, the linearly unstable base flow develops two or more identical vortices, depending on the values of α. The centers of these vortices are symmetrically positioned in the vertices of an equilateral polygon. In the case when the base flow is anticlockwise near the inner and clockwise near outer cylinders, the flow in each vortex rotates clockwise while the entire system of vortices drifts as a solid body anticlockwise. However, the drift direction may vary with the Reynolds number. The total flow field in the system with fully developed vortices strongly resembles a superposition of the purely azimuthal base flow and the flow field of the leading perturbation mode.

To validate theoretical results, we performed a series of experiments with horizontal soap films in an approximately piecewise-constant magnetic field produced by two concentric ring magnets with opposite polarity. The ratio of the radii of the film edges in the experimental setup was fixed to $\frac{r_1}{r_2} \approx 0.28$, which translates into $\alpha = \frac{r_1}{r_2 - r_1} \approx 0.38$. The vertical component of the magnetic field reversed its direction approximately at the midpoint in the gap between the inner and the outer magnets at the distance of $r \approx 26$ mm from the center. When the current of 200–300 mA was flowing through the film, stable vortex structures were observed at the inflection point of the azimuthal base flow velocity profile. We observed the formation of one large and three smaller satellite vortices arranged in a square pattern similar to that shown in Fig. 11 at $\alpha = 0.8$. Note that, for $\alpha = 0.38$, the model predicts either one vortex in the case of perfect-slip boundaries or two vortices for no-slip boundaries. Such a discrepancy between experimental and computational results is likely to be due to the difference in spatial distributions of real and model magnetic fields.

Finally, we note that the estimated values of the experimental Reynolds numbers at which the formation of vortices in an approximately piecewise-constant magnetic field was observed are somewhat smaller than those determined by the linear stability analysis (see Fig. 7). This may suggest the existence of subcritical bifurcations. Our preliminary nonlinear stability analysis indeed supports this hypothesis. The details of such an analysis will be reported elsewhere.

ACKNOWLEDGMENT

This research was partially supported by Grant No. DP250100868 from the Australian Research Council.

APPENDIX: LINEAR STABILITY OF AN UNFORCED FILM FLOW

For $W = 0$, Eq. (18) splits into two coupled second-order equations:

$$\tilde{\lambda}_n \tilde{\omega} = \Delta \tilde{\omega}, \tag{A1}$$

$$\tilde{\omega} = -\Delta \tilde{\psi}. \tag{A2}$$

Nontrivial solutions of Eq. (A1) in the interval $\alpha < r < 1 + \alpha$ only exist for negative real eigenvalues $\tilde{\lambda}_n < 0$,

$$\tilde{\omega} = C_1 J_n\left(r\sqrt{-\tilde{\lambda}_n}\right) + C_2 Y_n\left(r\sqrt{-\tilde{\lambda}_n}\right), \tag{A3}$$

where J_n and Y_n are Bessel functions of the first and second kind, respectively.

The stream function is found by integrating Eq. (A2) and is given by

$$\tilde{\psi} = -\frac{1}{\tilde{\lambda}_n}(\tilde{\omega} + C_3 + C_4 \ln r) \tag{A4}$$

for $n = 0$ and

$$\tilde{\psi} = -\frac{1}{\tilde{\lambda}_n}(\tilde{\omega} + C_3 r^n + C_4 r^{-n}) \tag{A5}$$

for wave numbers $n > 0$. The spectrum $\tilde{\lambda}_n$ is obtained from Eq. (19) as the solvability condition for constants C_i, $i = 1, 2, 3, 4$.

[1] G. R. Flierl, Isolated eddy models in geophysics, Annu. Rev. Fluid Mech. **19**, 493 (1987).

[2] M. V. Melander, N. J. Zabusky, and J. C. Mcwilliams, Symmetric vortex merger in two dimensions: Causes and conditions, J. Fluid Mech. **195**, 303 (1988).

[3] X. J. Carton, G. R. Flierl, and L. M. Polvani, The generation of tripoles from unstable axisymmetric isolated vortex structures, Europhys. Lett. **9**, 339 (1989).

[4] V. I. Arnold and L. D Meshalkin, The seminar of A. N. Kolmogorov on selected topics in analysis (1958–1959), Usp. Mat. Nauk **15**, 247 (1960).

[5] Y. Couder, The observation of a shear flow instability in a rotating system with a soap membrane, J. Phys. Lett. **42**, 429 (1981).

[6] V. M Ponomarev, Stability of a class of axisymmetric flows of an incompressible liquid, Fluid Dyn. **15**, 1 (1980).

[7] V. A. Dovzhenko, A. M. Obukhov, and V. M Ponomarev, Generation of vortices in an axisymmetric shear flow, Fluid Dyn. **16**, 510 (1981).

[8] G. K. Batchelor, *An Introduction to Fluid Dynamics* (Cambridge University Press, Cambridge, U.K., 1967).

[9] V. A. Romanov, Stability of plane-parallel Couette flow, Funct. Anal. Appl. **7**, 137 (1973).

[10] G. I. Taylor, VIII. Stability of a viscous liquid contained between two rotating cylinders, Philos. Trans. R. Soc. London, Ser. A **223**, 289 (1923).

[11] A. M. Obukhov, Kolmogorov flow and laboratory simulation of it, Russ. Math. Surv. **38**, 113 (1983).

[12] E. Fylladitakis, Kolmogorov flow: Seven decades of history, J. Appl. Math. Phys. **6**, 2227 (2018).

[13] P. R. Gent and J. C. Mcwilliams, The instability of barotropic circular vortices, Geophys. Astrophys. Fluid Dyn. **35**, 209 (1986).

[14] C. E. Leith, Minimum enstrophy vortices, Phys. Fluids **27**, 1388 (1984).

[15] B. Legras, P. Santangelo, and R. Benzi, High-resolution numerical experiments for forced two-dimensional turbulence, Europhys. Lett. **5**, 37 (1988).

[16] H. Lamb, *Hydrodynamics*, Cambridge Mathematical Library (Cambridge University Press, Cambridge, U.K., 1993).

[17] E. J. Hopfinger and G. J. F. van Heijst, Vortices in rotating fluids, Annu. Rev. Fluid Mech. **25**, 241 (1993).

[18] G. R. Flierl, On the instability of geostrophic vortices, J. Fluid Mech. **197**, 349 (1988).

[19] V. B. Levin, Free rotating layer of an electrically conducting fluid in an axial magnetic field, Magnetohydrodynamics **16**, 86 (1980).

[20] A. A. Klyukin and V. B. Levin, The stability of a free rotating layer in an electrically conducting fluid in an axial field, Fluid Dyn. **19**, 815 (1984).
[21] Kh. E. Kalis and Y. B. Kolesnikov, Stability of a rotating transverse axisymmetric flow in an axial magnetic field, Magnetohydrodynamics **3**, 72 (1983).
[22] A. Potherat, J. Sommeria, and R. Moreau, An effective two-dimensional model for MHD flows with transverse magnetic field, J. Fluid Mech. **424**, 75 (2000).
[23] N. F. Bondarenko, M. Z. Gak, and F. V. Dolzhanskiy, Laboratory and theoretical models of plane periodic flows, Izv. Akad. Nauk SSSR. Fyz. Atmos. Okeana **15**, 1017 (1979).
[24] A. M. Batchaev and V. M. Ponomarev, Experimental and theoretical investigation of Kolmogorov flow on a cylindrical surface, Fluid Dyn. **24**, 675 (1990).
[25] J. Sommeria, Experimental study of the two-dimensional inverse energy cascade in a square box, J. Fluid Mech. **170**, 139 (1986).
[26] Y. Couder, Two-dimensional grid turbulence in a thin liquid film, J. Phys. Lett. **45**, 353 (1984).
[27] Y. Couder, J.-M. Chomaz, and M. Rabaud, On the hydrodynamics of soap films, Physica D **37**, 384 (1989).
[28] J.-M. Chomaz, The dynamics of a viscous soap film with soluble surfactant, J. Fluid Mech. **442**, 387 (2001).
[29] R. C. C. Gomez, Response of a soap film to a continuous electromagnetic forcing, J. Visualization **20**, 87 (2017).
[30] H. Manikantan and T. M. Squires, Surfactant dynamics: Hidden variables controlling fluid flows, J. Fluid Mech. **892**, P1 (2020).
[31] I. Kim and S. Mandre, Marangoni elasticity of flowing soap films, Phys. Rev. Fluids **2**, 082001(R) (2017).
[32] N. S. Lalli and A. Giusti, Thin film modelling of magnetic soap films, J. Fluid Mech. **986**, A7 (2024).
[33] A. Figueroa, F. Demiaux, S. Cuevas, and E. Ramos, Electrically driven vortices in a weak dipolar magnetic field in a shallow electrolytic layer, J. Fluid Mech. **641**, 245 (2009).
[34] J. Pérez-Barrera, A. Ortiz, and S. Cuevas, Analysis of an annular MHD stirrer for microfluidic applications, in *Recent Advances in Fluid Dynamcis with Environmental Applications*, edited by J. Klapp, L. D. G. Sigalotti, A. Medina Ovando, A. López Villa, and G. Ruíz Chavarría (Springer, Berlin, 2016), pp. 275–288.
[35] A. Pototsky and S. A. Suslov, Electromagnetically driven flow in unsupported electrolyte layers: Lubrication theory and linear stability of annular flow, J. Fluid Mech. **984**, A75 (2024).
[36] A. Pototsky and S. A. Suslov, Effect of the dynamic contact angle on electromagnetically driven flows in free liquid films, Phys. Fluids **36**, 072111 (2024).
[37] K. J. Mysels, *Soap Films: Studies of Their Thinning and a Bibliography* (Pergamon Press, New York, 1959).
[38] M. Barigou and J. F. Davidson, Soap film drainage: Theory of experiment, Chem. Eng. Sci. **49**, 1807 (1994).
[39] E. Doedel, A. Champneys, T. Fairgrieve, Yu. Kuznetsov, B. Sandstede, and X. Wang, AUTO97: continuation and bifurcation software for ordinary differential equations (with HomCont), Technical report, (Concordia University, Montreal, Canada, 1999).
[40] B. Krauskopf, H. M. Osinga, and J. Galan-Vioque, *Numerical Continuation Methods for Dynamical Systems: Path Following and Boundary Value Problems* (Springer, Dordrecht, 2014).
[41] S. A. Orszag, Accurate solution of the Orr-Sommerfeld stability equation, J. Fluid Mech. **50**, 689 (1971).
[42] P. Drazin and W. Reid, *Hydrodynamic Stability* (Cambridge University Press, Cambridge, U.K., 1981).
[43] Q. He and X.-P. Wang, The effect of the boundary slip on the stability of shear flow, Z. Angew. Math. Mech. **88**, 729 (2008).
[44] J. L. Guermond, P. Minev, and J. Shen, An overview of projection methods for incompressible flows, Comput. Methods Appl. Mech. Eng. **195**, 6011 (2006).
[45] J. Olvera-Orozco, O. Suárez, G. Ramírez, J. Pérez-Barrera, A. Figueroa, and S. Cuevas, Electromagnetically driven flow in a soap film in an annular configuration (unpublished).
[46] W. Thielicke and E. J. Stamhuis, PIVlab—towards user-friendly, affordable and accurate digital particle image velocimetry in MATLAB, J. Open Res. Softw. **2**, e30 (2014).